ADVANCED FUNCTIONAL MATERIALS
www.afm-journal.de

All-In-One Hardware Devices with Event-Based Vision Sensor Arrays for Image Sensing, Computing, and Learning

Sen Zhang, Pingdan Xiao, Xitong Hong, Ruohao Hong, Chang Liu, Qianlei Tian, Wanhan Su, Chao Ma, Xingqiang Liu, Kenli Li, Johnny C. Ho, Yawei Lv, Qinghui Hong, Lei Liao,* and Xuming Zou**

Metal oxide semiconductors (MOSs) are considered as potential candidates for the low-cost, large-area fabrication of flexible optoelectronic devices. However, the current optoelectronic devices based on MOSs are limited to unidirectional photoresponse, which constrains the performance of MOSs-based vision sensors for artificial vision systems. Herein, for the first time, a flexible artificial vision system integrated with optical perception, computation, and learning functionalities is demonstrated using SnO optoelectronic synaptic transistor-based event-driven vision sensors to enable dynamic image perception, noise reduction, detection, and recognition. Specifically, an ambipolar SnO transistor is demonstrated by introducing HfO_2 passivation layer, which facilitates the movement of O atoms around Sn-vacancy sites to the HfO_2 layer to achieve the transformation from p-type to ambipolar transport behaviors. More importantly, the HfO_2-passivated SnO transistors exhibit gate-tunable bidirectional photoresponse behavior, which is essential to simulate the neurobiological functionalities of bipolar cells. This way, the multilayer neural network learning circuit built from SnO transistors achieves fast recognition at a 16% Gaussian noise level and high recognition accuracy up to 95.2% for pattern letters. Under the bending states, recognition accuracies are still retained at 91.2%. These properties are well retained even under the influence of 100% offset of the synaptic programming value.

1. Introduction

The current artificial vision sensors and systems usually generate lots of redundant data from a series of frame-based visual information processing. This massive amount of data would inevitably limit the application and development of these vision systems with increasing demand for real-time, automatic, and efficient information processing.[1–3] In comparison, the human retina can simultaneously detect and process visual information and substantially accelerates motion detection and recognition through integrated signal sensing, processing, and learning of advanced visual systems. Therefore, this phenomenon has inspired the development of electronic devices-based event cameras for artificial visual systems.[4,5] Recently, memristive devices have attracted extensive interest due to the similar structure and transmission characteristics between memristors and neural synapses.[4,6] It is worth mentioning that conventional memristor-based electronic synapses typically mimic the basic functionalities of synapses and neurons by solely applying electric stimuli.[7] This electric-modulated mode makes the corresponding devices insufficient to simulate the human visual system (HVS) realistically since the human retina is more sensitive to light stimuli of the outside world than electric stimuli.[8,9] To avoid these problems, novel synaptic devices that can efficiently integrate the light and electric stimuli co-modulation are urgently needed.[10]

S. Zhang, X. Hong, R. Hong, C. Liu, Q. Tian, W. Su, C. Ma, Y. Lv, X. Zou
Key Laboratory for Micro/Nano Optoelectronic Devices of Ministry of Education & Hunan Provincial Key Laboratory of Low-Dimensional Structural Physics and Devices
School of Physics and Electronics
Hunan University
Changsha 410082, P. R. China
E-mail: zouxuming@hnu.edu.cn

P. Xiao, K. Li, Q. Hong
College of Computer Science and Electronic Engineering
Hunan University
Changsha 410082, P. R. China
E-mail: hongqinghui@hnu.edu.cn

X. Liu, L. Liao
State Key Laboratory for Chemo/Biosensing and Chemometrics
College of Semiconductors (Integrated Circuits)
Hunan University
Changsha 410082, P. R. China
E-mail: liaolei@whu.edu.cn

J. C. Ho
Department of Materials Science and Engineering
City University of Hong Kong
Kowloon, Hong Kong SAR 999077, P. R. China

The ORCID identification number(s) for the author(s) of this article can be found under https://doi.org/10.1002/adfm.202306173

DOI: 10.1002/adfm.202306173

Because of the unique light-matter interaction, optoelectronic synaptic transistors are advantageous, compared to memristive devices, in providing long-term device stability, efficient integration of different stimuli, and the capability of simultaneously performing different kinds of artificial vision functions.[11,12] At present, optoelectronic synaptic transistors based on various kinds of photosensitive materials and hybrid structures with inherent persistent photoconductivity have been extensively achieved, such as quantum dots,[13] 2D materials,[14] oxide semiconductors,[15,16] and halide perovskites.[17] In particular, oxide semiconductors materials have been considered as potential candidates for the low-cost, large-area fabrication of flexible optoelectronic devices owing to their unique optical transparency properties, high conductivity, and easy integration in a single material.[18] For instance, vision sensors based on different oxide semiconductors, including In_2O_3,[19] IGZO,[20] ZnO,[21] and Ga_2O_3,[22] have been demonstrated for artificial vision systems. Nevertheless, achieving the event camera would require displaying the on and off events using excitatory and inhibitory modulations (bidirectional photoresponse modulations) by all-photonic stimulation.[23] However, the current artificial vision sensors based on oxide semiconductors are limited to unidirectional photoresponse, which constrains the development of vision sensors for artificial vision systems. Until now, to the best of our knowledge, artificial vision systems based on oxide semiconductors-implemented event cameras remain unexplored.

Herein, for the first time, a flexible artificial vision system integrated with optical perception, computation, and learning functionalities is proposed. Specifically, SnO-based optoelectronic synaptic transistors are employed as event-driven vision sensors to enable dynamic image perception, noise reduction, detection, and recognition. One of the key developments is the utilization of the HfO_2 passivation layer for the SnO devices. The density functional theory (DFT) calculations reveal that this passivation could facilitate the movement of O atoms around Sn-vacancy sites to the HfO_2 layer to achieve the transformation from p-type to ambipolar transport behaviors in SnO. More importantly, through the utilization of the gate-tunable bidirectional photoresponse capable of this HfO_2-passivated SnO transistor under a light illumination of 457 nm, the neurobiological functionalities of bipolar cells are successfully simulated by a single device. This way, in each recognition progress, the multilayer neural network learning circuit built from SnO transistors achieves fast recognition at a 16% Gaussian noise level and high recognition accuracy up to 95.2% for pattern letters. The recognition accuracies at the bending state can still retain 91.2%. Benefiting from the good stability and reliability of the flexible SnO optoelectronic transistor, these properties are well retained under the influence of 100% offset of the synaptic programming value, demonstrating considerable prospects in wearable devices and artificial vision system. Ultimately, the study establishes the development of an all-in-one artificial vision system to enable dynamic image perception, noise reduction, detection, and recognition, thus demonstrating the great potential of SnO optoelectronic transistors in realizing compact and efficient artificial vision systems.

2. Results and Discussion

In general, the human retina contains various kinds of neurons, including photoreceptors, bipolar cells, and ganglion cells.[24] The vision information is received by photoreceptors and transmitted to the bipolar cells to generate positive or negative electrical signals and eventually to the brain, significantly improving process speed in the brain.[1] Bipolar cells can be classified into ON-bipolar and OFF-bipolar cells, which respond to light stimuli with a bidirectional photoresponse. In order to mimic the neurobiological functionalities of bipolar cells, we propose to develop a flexible optoelectronic synapse based on the SnO transistor, as illustrated in **Figure 1**a. An optical image of the flexible device array on the PI substrate is depicted in Figure 1a inset. The fabrication process of the SnO optoelectronic synaptic transistor array is schematically shown in Figure S1 (Supporting Information). Briefly, a 20 nm-thick SnO film was deposited by radiofrequency (RF) sputtering at room temperatures in a reactive Ar/O_2 gas atmosphere. Next, the Cr/Au (10/50 nm) source-drain electrodes were evaporated on the SnO film by thermal evaporation, and the HfO_2 layer with a thickness of 10 nm was deposited by the atomic layer deposition (ALD) process at 95 °C. In particular, the direct growth of HfO_2 passivation layer, and then the annealing treatment was processed at 350 °C for 10 min in ambient air, which facilitates the introduction of the metallic Sn-related defect states and transition of the channel polarity.[25] From a high-resolution transmission electron microscopy (HR-TEM) image and corresponding energy dispersive X-ray spectroscopy (EDS) line-scanning elemental mapping of a cross-sectional region of the SnO optoelectronic transistor (Figure S2a,b, Supporting Information), the thickness of SnO and HfO_2 is further confirmed, and the spatial distributions of the atomic contents directly show the stack structure of device, consistent with the HR-TEM image.

To evaluate the optoelectrical characteristics of our proposed SnO transistors, the transfer characteristic curves of the un-passivated and HfO_2-passivated SnO transistors under dark and at various light intensities were measured at a constant drain voltage of $V_{ds} = -1$ V. As shown in Figure 1b, the un-passivated SnO transistor exhibits a typical p-type transistor characteristic, showing a unidirectional photocurrent response under a light illumination of 457 nm. In contrast, the HfO_2-passivated SnO transistor exhibits the ambipolar transport behavior under dark and gate-tunable bidirectional photoresponse behavior under a light illumination of 457 nm. As shown in Figure S3a (Supporting Information), a significant shift of transfer curves toward the positive direction and increased off-state current after light illumination operation with various intensities were observed, suggesting that the photogating and photoconductive effects dominated the photocurrent generation of the ambipolar SnO transistor.[26] The transfer curves are gradually shifted toward the positive direction after light illumination, indicating the photoexcited electrons trapped in the HfO_2 layer and leaving extra holes in the SnO conducting channel, thereby contributing to an increase in photocurrent. This transformation from p-type to ambipolar transport behaviors under introducing HfO_2 passivation layer provides a physical foundation for achieving a bidirectional photoresponse, which is significant for mimicking the biological characteristics

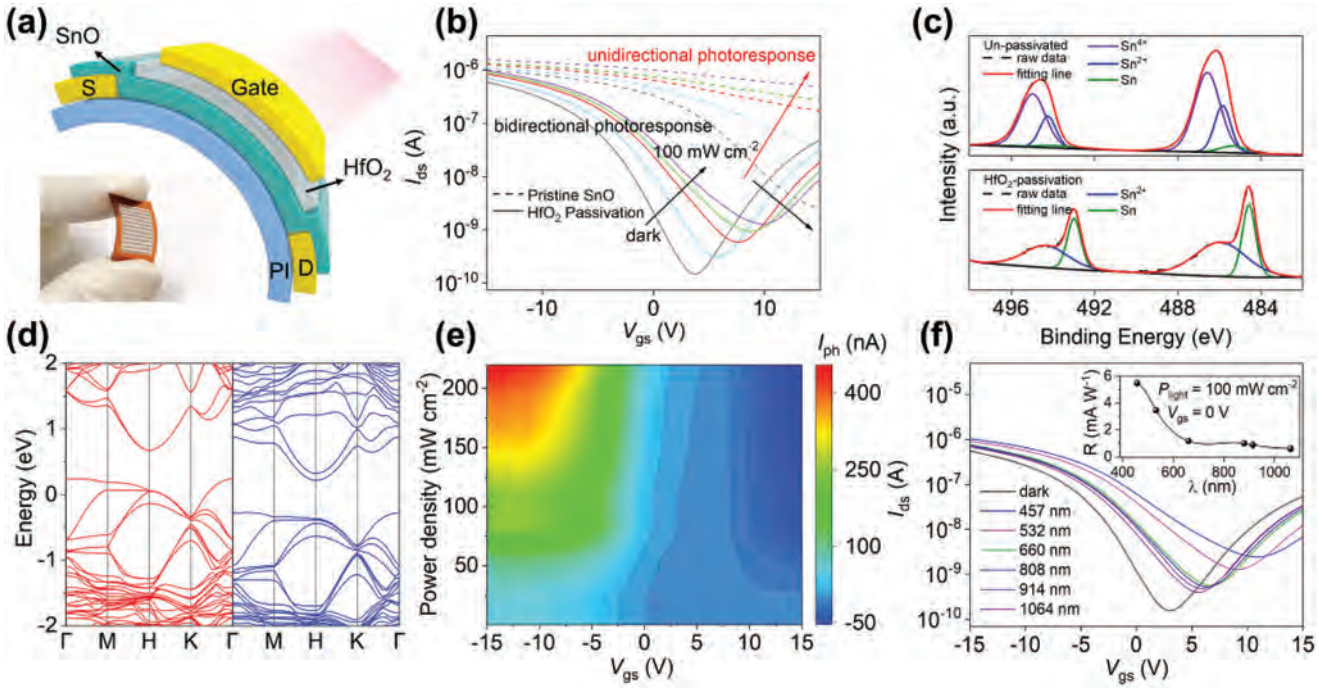

Figure 1. Schematic diagram and optoelectronic characteristics of flexible artificial synapses based on SnO/HfO_2 transistors. a) Schematic diagram of the structure of the artificial synaptic device. The inset depicts an optical image of the device array. b) Transfer characteristic curves of the pristine SnO and SnO/HfO_2 synaptic transistors measured at $V_{ds} = -1$ V under different light intensities. c) XPS of Sn 3d in un-passivated and HfO_2 passivated SnO film. d) The band structures of Sn-vacancy (left) and Sn-O-vacancy (right) SnO. e) P_{light} and V_{gs} dependent photocurrent extracted from the transfer characteristic curves shown in (b). f) Transfer characteristic curves at different wavelengths. The inset depicts the curve between photoresponsivity and incident light wavelengths at the same light intensity of 100 mW cm^{-2}.

of bipolar cells. To further evaluate the photoresponse performance of the optoelectronic synaptic transistor, photoresponsivity (R) can be calculated according to the following equation:[27,28]

$$R = \frac{\left|I_{light} - I_{dark}\right|}{P_{light} \times S} = \frac{\left|I_{ph}\right|}{P_{light} \times S} \quad (1)$$

where I_{dark} and I_{light} are output current under dark and light illumination, respectively, P_{light} is incident light intensity, S is effective illuminated area, and I_{ph} refers to photocurrent. As shown in Figure S3b (Supporting Information), it is obvious that the photoresponsivity is dependent on the input light intensity and decreases with increasing light intensity. Specifically, according to the Equation (1), the photoresponsivity value of up to 11.5 A W^{-1} can be obtained at $V_{gs} = -15$ V under 457 nm incident laser with a light intensity of 0.04 mW cm^{-2} at −1 V bias. X-ray photoelectron spectroscopy (XPS) measurements were carried out to investigate the chemical bonding state and chemical composition of the un-passivated and HfO_2-passivated SnO films, and the corresponding results are given in Figure 1c. Here, the HfO_2 passivation layer is speculated to introduce metallic Sn-related states, enabling the transformation from p-type to ambipolar conducting behaviors in SnO.[25] The typical wide survey XPS spectra of the un-passivated and HfO_2-passivated SnO films are given as shown in Figure S4 (Supporting Information). The XPS analysis gave the surface atomic percentages of O and Sn elements in the SnO films (Table S1, Supporting Information). The Sn/O atomic ratio of the un-passivated SnO films is lower than that of the HfO_2-passivated SnO films, suggesting the O movement of SnO induced by the HfO_2 passivation layer.

The transformation from p-type to ambipolar transport behaviors in SnO after the HfO_2 passivation can be justified by the DFT calculation. As shown in Figure S5 (Supporting Information), the p-type behavior in SnO is induced by the Sn vacancy, whereas the passivation could move the O atoms near the vacancy to the HfO_2 layer due to the strong reducibility of the Hf atoms, releasing an energy of 3.8–5.04 eV during the O movement. The band structures of Sn-vacancy and Sn–O-vacancy containing SnO from the DFT calculation are given in Figure 1d, in which the p-type and intrinsic doping effects are observed, verifying that the O movement induced a transport variation. Significantly, owing to the V_{gs} and P_{light} dependence of the photocurrent (Figure 1e), the ambipolar SnO transistor exhibits a gate-tunable positive photocurrent (PPC) and negative photocurrent (NPC) under light illumination of the 457 nm laser, enabling mimicking the neurobiological functionalities of bipolar cells during visual information processing in the human retina. In addition, different optoelectronic performances were observed when the ambipolar SnO transistor was focused on light illumination with the same light intensity of 100 mW cm^{-2} but with various wavelengths, as illustrated in Figure 1f. The inset in Figure 1f depicts the photoresponsivity as a function of the incident light wavelengths; the ambipolar SnO transistor exhibits broadband photoresponse in the wavelength range from 457 to 1064 nm, which is consistent with the absorption

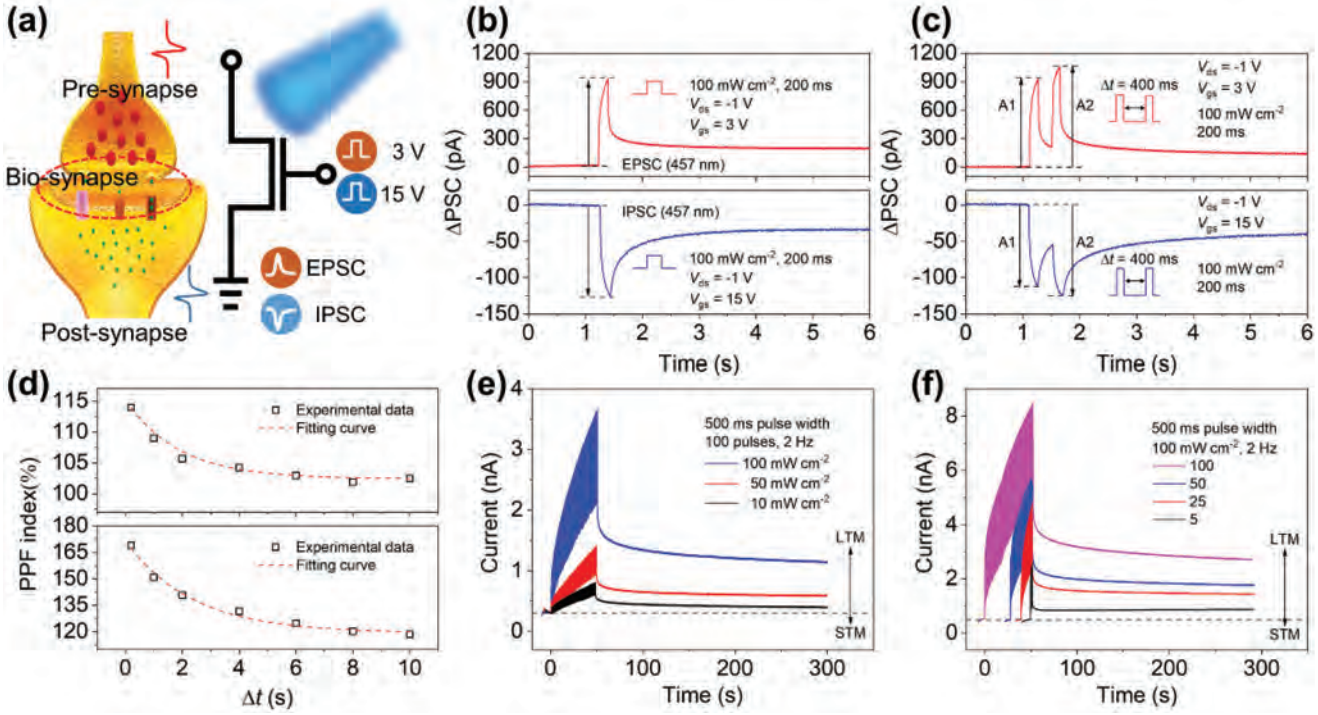

Figure 2. Optoelectronic modulated synaptic plasticity performance and mimicry of artificial visual memory. a) Schematic diagram and simplified electrical circuit of biological synapses. b) EPSC and IPSC of the device triggered by light stimuli with 457 nm wavelength (100 mW cm^{-2}, 200 ms) at V_{gs} = 3 V and V_{gs} = 15 V, respectively. c) PPF of the device triggered by the successive pulses with 457 nm wavelength. d) The curve of the PPF index and interval time between paired successive pulses. The transition from STM to LTM was realized by changing e) the light intensity and f) the number of pulsed light stimuli.

spectrum of HfO_2-passivated SnO films (Figure S6, Supporting Information).

As a specialized structure of the nerve system, a synapse consists of the presynaptic membrane, the synaptic cleft, and the postsynaptic membrane. Electrical stimulation in the presynapse is converted into the release of excitatory/inhibitory neurotransmitters that blinds the receptors on the postsynapse, leading to the excitatory/inhibitory postsynaptic current (EPSC/IPSC), as presented in **Figure 2**a.[29,30] Due to the gate-tunable NPC and PPC, our optoelectronic synapse has a significant potential to mimic various synaptic plasticity. As displayed in Figure 2b, the modulation of V_{gs} to 3 and 15 V generated opposite results by applying light stimuli with a wavelength of 457 nm (100 mW cm^{-2}, 200 ms), which were triggered to increase and decrease the photocurrent in the optoelectronic synapse to mimic both EPSC and IPSC, respectively. In the biological neural system, paired-pulse facilitation (PPF) is one of the important synaptic functionality, which is regarded as an essential form for recognizing and decoding temporary information.[15,30] The evaluation of PPF behaviors using the SnO/HfO_2 optoelectronic synapse is demonstrated by applying two successive light stimuli with a time interval Δt, wherein two pulses had a width of 0.2 s and a light intensity of 100 mW cm^{-2}. Figure 2c indicates that the EPSC and IPSC triggered by the second light spike (A_2) are significantly enhanced than that triggered by the first light spike (A_1) because of the accumulation of trapped photogenerated electrons in the HfO_2 layer. As shown in Figure 2d, the PPF index (A_2/A_1) reduces with the increase of Δt, where the red dashed line is the result of fitting using a double exponential decay function, which agrees well with the measured data. The relationship between the PPF index and the Δt can be fitted by the following double exponential decay function:[31]

$$\text{PPF index} = C_1 \exp\left(-\frac{\Delta t}{\tau_1}\right) + C_2 \exp\left(-\frac{\Delta t}{\tau_2}\right) + C_0 \quad (2)$$

where C_0 is 100%, which means that the PPF index gradually converges to 100%, C_1 and C_2 are the initial facilitation magnitudes of the rapid and slow respective phases, and τ_1 and τ_2 are the characteristic relaxation time of the rapid and slow decay terms, respectively. Moreover, the fitted values of τ_1 and τ_2 for the EPSC/IPSC are 1.70/0.58 s (τ_1) and 2.08/4.80 s (τ_2), respectively. The corresponding values of τ_1 and τ_2 are similar to the biological synapse, indicating that our optoelectronic synapse has good potential for simulating the PPF behaviors of biological synapses. Another important synaptic functionality is the operational transition from short-term memory (STM) to long-term memory (LTM), also known as memory consolidation, which can be realized by simply increasing the number and frequency of pulses.[7,32] In Figure 2e,f and Figure S7 (Supporting Information), the increase in intensity, number, and frequency of pulsed light stimuli has been applied on the device, resulting in both a higher peak current and retained memory, which demonstrate that the transition from STM to LTM can be successfully simulated in our optoelectronic synapse. With the above frequency-modulated photocurrent response

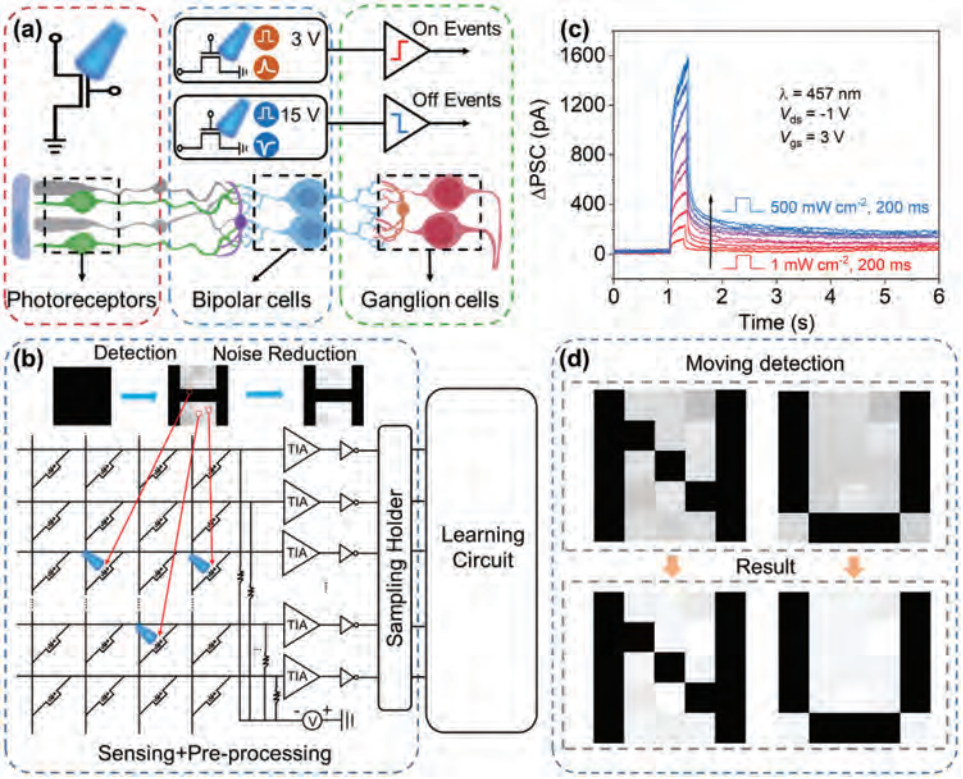

Figure 3. Illustration of the event-based visual sensor array for motion detection. a) Three-layer model of the human retina and the corresponding event-based visual sensor pixel circuit. b) Hardware device circuit design of the event-based visual sensor array for image sensing and pre-processing. c) EPSC under the light with various light intensities from 1 to 500 mW cm^{-2}, followed by current decay after the light is off. d) Results after detection and pre-processing of dynamic images.

characteristics (Figure S7, Supporting Information), the interest-modulated visual memory effect has been well mimicked, as shown in Figure S8 (Supporting Information). Compared with neuromorphic characteristics of the optoelectronic synapse under short-wavelength light exposure, various synaptic plasticity under long-wavelength light exposure have also been well mimicked, as shown in Figure S9a–e (Supporting Information).

Retina-inspired artificial vision systems, which can simulate the biological functions of the HVS, have been extensively developed because they can combine image sensing, real-time information processing, pattern recognition, and learning.[33,34] The HVS is composed of the retina, optic nerve, and visual cortex in the brain; the retina receives and converts light signals to electrical output signals. After light signals are pre-processed in the retina, these signals are transmitted to the visual cortex in the brain through the optic nerve, where visual information can be further processed to realize the functions of recognition, memory, and learning.[35] The event camera pixel models a simplified three-layer retina in the human eye by mimicking the optic nerve information flow, which consists of the cone or rod photoreceptor cells, on/off bipolar cells, and on/off ganglion cells (**Figure 3**a).[36] This structure is replicated by introducing optoelectronic synapses, and the circuit implementation is shown in Figure 3a. The event camera contains a SnO/HfO_2 optoelectronic synaptic transistor inspired by the bipolar cells of the human eye, which can generate a gate-tunable bidirectional optical response after sensing an optical stimulus, successfully simulating the biological function of the bipolar cells and the co-modulation of optical and electrical operations. Each pixel works independently and automatically triggers an ON or OFF event when the light intensity changes. By constructing the visual sensing array based on optoelectronic synapses with positive and negative response conductivities, the array can achieve image detection and pre-processing to mimic the functions of the human retinal, as shown in Figure 3b. First, the moving process of the dynamic image is detected with an event camera, which only records the image brightness if there is a relative change in the intensity of a pixel. After memorizing its static image, it is combined with a visual sensor array to calculate the differences of image brightness at the moment of t and $t+\Delta t$, enabling dynamic image detection and noise reduction. Then, the optoelectronic transistors perceive different light stimuli to generate different photoresponse currents, which are converted to voltage signals by trans-impedance amplifiers (TIA) before being digitized by the sampling holder. In the proposed device array and corresponding peripheral circuit, with the help of peripheral circuits in devices array, the set voltage source and TIA achieve can extract information from moving images based on Kirchhoff's law and the characteristics of amplifiers (high input resistance and high open-loop gain), and thus TIA can the current of extracted information convert to voltage signals which facilitate later operation. Since the proposed device array is to process dynamic images, the sampling holder is designed to connect with device array, which not only achieves maintenance of the input voltage signal,

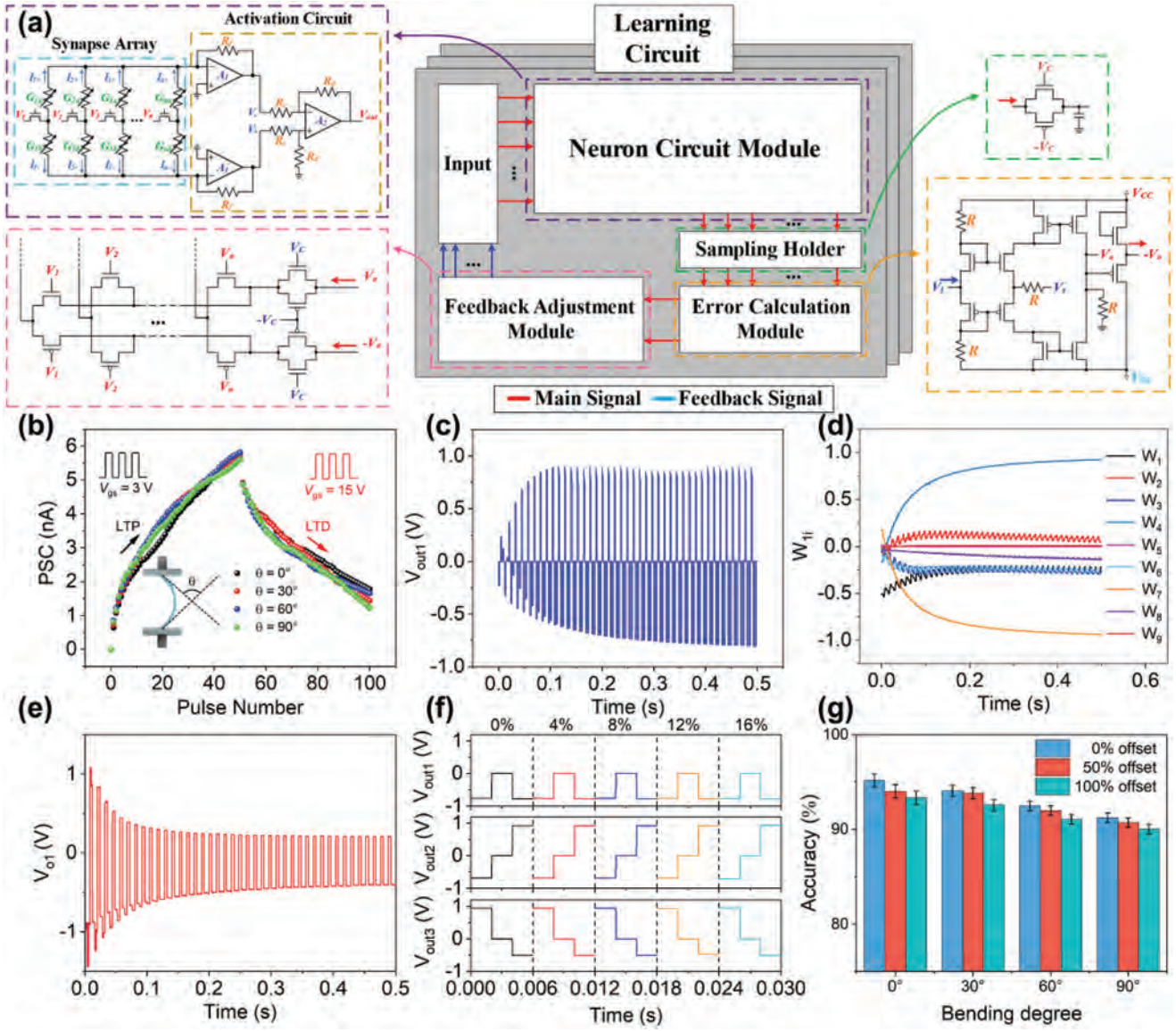

Figure 4. Design principle and simulation of the self-learning circuit. a) Schematic diagram of a neuronal circuit design based on optoelectronic synapses that enable automatic online learning on-chip. b) LTP and LTD cycles of artificial synapses in flat and bending states. Simulation results of self-learning neuron circuit training, c) feedforward calculation, d) feedback adjustment, and e) error calculation. Test results on original and noisy image inputs, f) are the output results of each neuronal circuit. g) Accuracy of the simulation process in different states with offsetting the synaptic programming value.

but also is helpful for the next learning and recognition by using analog circuits. The pre-processed images are fed as voltage signals into a circuit-implemented multilayer neural network for on-chip learning. Figure 3c and Figure S9f (Supporting Information) show the modulation effect of light intensity on the EPSC, indicating that the conductance decay trend depends on the light intensity. When irradiated at higher intensities, the conductance gradually decreases when the light is turned off and eventually remains relatively high above the initial state (Figure S10, Supporting Information), which can be considered as LTM. We detect the dynamic images using this property and further pre-process the captured static images. Three different pattern letters ("H," "N," and "U") are proposed in the simulation experiment, each pattern letter is composed of a 5 × 5 binary image, which can be described as 25 binary inputs x_1–x_{25}. The results of pre-processed static images as voltage signals in the pixel-based vision sensor array are shown in Figure 3d and Figure S9g (Supporting Information), indicating that the pre-processed image noise is further reduced than the initial image; the pre-processed images are then passed in voltage signals into a multilayer neural network learning circuit for on-chip learning.

Generally, the learning circuit consists of neuron circuit module, sampling holder, error calculation module, feedback adjustment module, and input interface, as shown in **Figure 4**a. When the event-based vision sensor array captures information from the outside environment, the outdoor signal will be sensed, denoised, and converted into a voltage signal suitable for subsequent learning and recognition. The voltage signal first flows into

the synapse array of the neuron circuit module when the switch composed of the trans-impedance amplifier and resistors turn on. First, the working principle of the synapse array is as the following:[37]

$$V_{-} - V_{+} = R_f \times \left[\left(G_{1a} - G_{1b}\right) \times V_1 + \cdots + \left(G_{\mathrm{na}} - G_{\mathrm{nb}}\right) \times V_n\right] \tag{3}$$

where V_{-} and V_{+} are the respective input voltages of the operational amplifiers (hereafter referred to as OAs); $G_{\mathrm{na,\,b}}$ and V_{n} represent the weight parameter of the learning algorithm and input signal, respectively; R_{f} and OAs consist of the trans-impedance amplifier (hereafter referred to as TIA), which can transform input current into voltage. According to Ohm's laws and Kirchhoff's law, the above equation can achieve multiplying and accumulating (henceforth referred to as MAC) of synapse for input signal and weight parameter. After the MAC operation for the input signal, the synapse will have a different output value based on the value of the signal. Therefore, the neuron circuit module would export different output voltages with the activation circuit. The operation principle of the activation circuit is as the following:

$$V_{\mathrm{out}} = \begin{cases} V_{\mathrm{DD}}, & V_{\mathrm{out}} < V_{\mathrm{DD}} \\ \dfrac{R_{\mathrm{d}}}{R_{\mathrm{f}}}\left(V_{-} - V_{+}\right), & V_{\mathrm{DD}} \le V_{\mathrm{out}} \le V_{\mathrm{CC}} \\ V_{\mathrm{CC}}, & V_{\mathrm{out}} > V_{\mathrm{CC}} \end{cases} \tag{4}$$

where V_{DD} and V_{CC} are the respective supply voltages of the operational amplifiers, R_{d}, R_{f} are the resistance of the activation circuit, the ratio of which can achieve control of the output signal value based on the working principle of OA and the subtraction circuit when V_{out} is in the range of $[V_{\mathrm{DD}}, V_{\mathrm{CC}}]$.

The sampling holder in Figure 4a can retain the input signal value from the neuron circuit module, which consists of the complementary metal-oxide-semiconductor (CMOS) switch and capacitor. When the control voltage V_{C} is positive and $-V_{\mathrm{C}}$ is a negative voltage, the CMOS switch turns on, the input signal charges the capacitors, and the output port of the sampling holder retains the input value. On the contrary, the capacitors will discharge when the switch turns off due to the negative V_{C} and the positive $-V_{\mathrm{C}}$. Based on the above analysis, the module can achieve the function of the holding voltage. The maintained voltage must be processed to learn further and recognize. The error calculation module can obtain the difference between the realistic and ideal signals, which corresponds to the cost function in the learning algorithm, facilitating subsequent self-adjustment, and learning. The module in Figure 4a is composed of CMOS transistors and resistances. It can achieve the comparison between the input value V_{i} and the ideal value V_{t}, and export the different value V_{o} and its corresponding negative value $-V_{\mathrm{o}}$. These results will be transmitted to the feedback adjustment module and the input interface in order to adjust the weight parameter and the consequent learning task.

The feedback adjustment module consists of transistors (including CMOS transistors), some of which compose the switches for controlling the result from the error calculation module. Moreover, the other transistors comprise a control cell similar to the above switch, which is connected to the input interface and synapse array using the feedback structure. After the switches of the synapse array turn on, the learning circuit is in the mode of weight adjustment. When the control signal V_{C} is positive, the switch turns on, and the signal flows into the feedback adjustment module. When the input signal V_{n} ($n = 1, 2, 3, \ldots$) is a positive voltage, the upper transistor will turn on, and the bottom transistor will turn off in Figure 4a; this way, the voltage V_{o} will be applied to the synapse array. On the contrary, a negative input signal V_{n} will turn the bottom transistor on and turn the upper transistor off; the voltage $-V_{\mathrm{o}}$ will be applied to the synapse array. The sign of V_{o} and $-V_{\mathrm{o}}$ determine whether the weight parameter increases or decreases, which achieves the above circuit's learning function. Based on the learning circuit, the whole neural network structure for the learning tasks is illustrated in Figure S11 (Supporting Information).

To adjust different synaptic weights of the visual sensing array, different conductance states can be obtained by applying multiple-pulse light stimuli to the optoelectronic synaptic transistor. Fifty consecutive pulse light stimuli with a wavelength of 457 nm were applied to the optoelectronic synapse at a gate voltage of 3 and 15 V, respectively; the long-term potentiation (LTP) and long-term depressing (LTD) cycles of the optoelectronic synapse in the flat and bending states are shown in Figure 4b. All neurons are connected to the next layer of neurons through the synaptic weight. The neural network's synaptic weight is considered the conductance difference between two optoelectronic synapses, and the experimental data are extracted from the LTP/LTD curves. Then, the whole training process was simulated by PSPICE. The learning and recognition results of the three learning circuits are shown in Figure 4c and Figure S12a,d (Supporting Information). The feedback adjustment results during each cycle are shown in Figure 4d and Figure S12b,e (Supporting Information). The error adjustment results during each cycle are shown in Figure 4e and Figure S12c,f (Supporting Information). The simulation results show that the training of the three learning neurons is synchronized. Feedforward computation and feedback adjustment are alternated in each learning circuit with parallel operations. As the training period increases, the output of the three learning neurons gradually approaches the target, while the error signal will gradually decrease. The training stops when the error obtained by the three neurons does not exceed the set threshold voltage representing the training target.

Figure 4f shows the simulation results of the learning circuit for the performance testing. The original training images are added to the trained multilayer neural network, and the corresponding outputs of neurons 1, 2, and 3 are shown in the first column of Figure 4f. The outputs of the three neurons are coincided with the desired outputs, indicating that the proposed learning circuit performs the image recognition task well. Later, 4–16% Gaussian noise is added to the input image, and the corresponding outputs are shown in the remaining columns of Figure 4f. Although there is a small deviation between the output and the expected value, the learning circuit still classifies the input images correctly due to the distinguishing voltage of 0 V. These results imply that the proposed learning circuit has good robustness to input signal fluctuation with the help of the adopted closed-loop circuit structure. Figure 4g shows the statistics of image recognition accuracy at different conditions. The recognition accuracies

of the learning circuit at different conditions can reach 95.2%, 94.1%, 92.5%, and 91.2%, respectively, and the recognition accuracy in the curved state is slightly different from that in the flat state. These findings indicate the considerable potential of the proposed optoelectronic synapse in developing a flexible artificial vision system. Since the initial values of the vision sensor array are set randomly, the device programming values exist within a certain degree of offset. The effect of different degrees of offsets on the recognition accuracy of the learning circuit is small, and the learning accuracy can still reach 93.3%, 92.6%, 91.1%, and 90.0%, demonstrating good robustness. The long-term potentiation (LTP) and long-term depressing (LTD) cycles of the optoelectronic synapse under a wavelength of 1064 nm are shown in Figure S9h (Supporting Information). Figure S9i (Supporting Information) shows the statistics of image recognition accuracy at different offsets under short-wavelength and long-wavelength light exposure, and the recognition accuracies of both are comparable.

3. Conclusion

In conclusion, our findings indicate that the developed system has the characteristics of integrating sensing, computing, and learning and also can realize dynamic image perception, noise reduction, detection, and recognition. Specifically, the SnO/HfO_2 optoelectronic synaptic transistor, inspired by the bipolar cells of the human eye, can realize the co-modulation of optical and electronic operations. It can also generate gate-tunable EPSC and IPSC optoelectronic properties, allowing for image noise reduction processing. More importantly, the visual sensing array constructed based on the optoelectronic synapses can achieve dynamic event-based image detection. A multilayer neural network learning circuit can further enable on-chip learning, making fast image detection and successful recognition possible. Our proposed event camera-based artificial vision system not only contributes to the development of event-based dynamic image detection technology but also offers the application possibility in the fields such as autonomous driving, robot control, and security monitoring.

4. Experimental Section

Device Fabrication: The SnO/HfO_2 optoelectronic synaptic transistors were fabricated on the PI substrate. The Cr/Au (10/50 nm) electrodes were patterned from bottom to top using thermal evaporation. Then, a 20 nm thick SnO film was deposited from a metallic Sn target onto the PI substrate by RF magnetron sputtering at room temperature with a single tin target (99.999%, HZAM). The deposition was conducted at a power of 38 W at room temperature under a pressure of 0.75 Pa. During the deposition, the oxygen partial pressure was 15%. The first annealing treatment was performed at 250 °C for 10 min in ambient air. After that, a 10 nm thick HfO_2 was deposited by ALD at 95 °C, and the growth rate of the HfO_2 films was 1.25 Å per cycle. The second annealing treatment was performed at 350 °C for 10 min in ambient air. Finally, the SnO/HfO_2 optoelectronic synaptic transistor arrays were realized by thermal evaporation of Cr/Au (10/50 nm) as the gate electrodes.

Material Characterization and Device Measurement: The high-resolution TEM image was obtained by JEOL JEM-2100F TEM/scanning TEM instrument operating at 200 kV, equipped with an Oxford INCA energy-dispersive spectroscopy detector and a Gatan Enfina EELS spectrometer for elemental mapping. The absorption spectrum was characterized by the UV–vis spectrometer (Shimadzu UV-2550). The chemical composition of SnO film was characterized by XPS. The electrical and optoelectrical measurements were measured by the semiconductor parameter analyzer (Agilent B1500A). The incident light sources were lasers with wavelengths of 457, 532, 660, 808, 914, and 1064 nm, respectively.

First-Principle Calculation: The DFT calculation was performed by an open-source code QUANTUM ESPRESSO.[38] The ultrasoft pseudopotentials were from the PSlibrary v1.0.0, and the Perdew–Burke–Ernzerhof (PBE) functionals were adopted.[39] The plane-wave cut-off energies were 47 Ry, according to the library suggestion. The structures were fully relaxed using the Broyden–Fletcher–Goldfarb–Shanno (BFGS) quasi-newton algorithm until the energy variation and atom forces in the three directions were smaller than 10^{-4} Ry and 10^{-4} Ry $Bohr^{-1}$, respectively. In the bulk SnO model, the unit cell was expanded by $3 \times 3 \times 2$ before the defect inducing, resulting an $11.59 \times 11.59 \times 9.83$ supercell size. The Fermi–Dirac smearing scheme was adopted with a smearing width of 0.026 eV to guarantee the accuracy of the Fermi level, and the Brillouin zone k-point sampling was $2 \times 2 \times 2$ at the electronic ground-state computations.

Simulation Method: The whole automatic online learning process of the learning circuit was simulated by PSPICE, and all data for the image sensing, computing, and learning processes came from realistic experimental metadata based on the SnO/HfO_2 optoelectronic synaptic transistor vision sensor.

Supporting Information

Supporting Information is available from the Wiley Online Library or from the author.

Acknowledgements

This work was supported by the National Key Research and Development Program of the Ministry of Science and Technology (Grant No. 2021YFA1200700, 2022YFB4400100), the China National Funds for Distinguished Young Scientists Grant 61925403, the China National Funds for Outstanding Young Scientists Grant 62122024, the National Natural Science Foundation of China (Grant Nos. 62134001, 12174094, 62274060, 62001163, and 62234008), the Natural Science Foundation of Hunan Province (Grant Nos. 2021RC5004, and 2021JJ20028), the Guangdong Basic and Applied Basic Research Foundation-Regional Joint Fund (2020B1515120040), the Shenzhen Science and Technology Research Funding (JCYJ20200109115408041), the Key Research and Development Plan of Hunan Province under Grant (Nos. 2022WK2001), and the Natural Science Foundation of Changsha (Grant Nos. kq2004002).

Conflict of Interest

The authors declare no conflict of interest.

Data Availability Statement

The data that support the findings of this study are available from the corresponding author upon reasonable request.

Keywords

event cameras, on-chip learning, optoelectronic synapses, SnO, vision sensors

Received: June 1, 2023
Revised: August 7, 2023
Published online: August 30, 2023

[1] C.-Y. Wang, S.-J. Liang, S. Wang, P. Wang, Z. a. Li, Z. Wang, A. Gao, C. Pan, C. Liu, J. Liu, *Sci. Adv.* **2020**, *6*, eaba6173.
[2] F. Wang, F. Hu, M. Dai, S. Zhu, F. Sun, R. Duan, C. Wang, J. Han, W. Deng, W. Chen, *Nat. Commun.* **2023**, *14*, 1938.
[3] F. Liao, F. Zhou, Y. Chai, *J. Semicond.* **2021**, *42*, 013105.
[4] Q. Wu, B. Dang, C. Lu, G. Xu, G. Yang, J. Wang, X. Chuai, N. Lu, D. Geng, H. Wang, *Nano Lett.* **2020**, *20*, 8015.
[5] Z. Zhang, S. Wang, C. Liu, R. Xie, W. Hu, P. Zhou, *Nat. Nanotechnol.* **2022**, *17*, 27.
[6] B. Sun, T. Guo, G. Zhou, S. Ranjan, Y. Jiao, L. Wei, Y. N. Zhou, Y. A. Wu, *Mater. Today Phys.* **2021**, *18*, 100393.
[7] X. Yan, J. Zhao, S. Liu, Z. Zhou, Q. Liu, J. Chen, X. Y. Liu, *Adv. Funct. Mater.* **2018**, *28*, 1705320.
[8] F.-S. Yang, M. Li, M.-P. Lee, I.-Y. Ho, J.-Y. Chen, H. Ling, Y. Li, J.-K. Chang, S.-H. Yang, Y.-M. Chang, *Nat. Commun.* **2020**, *11*, 2972.
[9] J.-L. Meng, T.-Y. Wang, L. Chen, Q.-Q. Sun, H. Zhu, L. Ji, S.-J. Ding, W.-Z. Bao, P. Zhou, D. W. Zhang, *Nano Energy* **2021**, *83*, 105815.
[10] S. Gao, G. Liu, H. Yang, C. Hu, Q. Chen, G. Gong, W. Xue, X. Yi, J. Shang, R.-W. Li, *ACS Nano* **2019**, *13*, 2634.
[11] K. Liang, R. Wang, B. Huo, H. Ren, D. Li, Y. Wang, Y. Tang, Y. Chen, C. Song, F. Li, *ACS Nano* **2022**, *16*, 8651.
[12] N. Ilyas, J. Wang, C. Li, D. Li, H. Fu, D. Gu, X. Jiang, F. Liu, Y. Jiang, W. Li, *Adv. Funct. Mater.* **2022**, *32*, 2110976.
[13] C. Jo, J. Kim, J. Y. Kwak, S. M. Kwon, J. B. Park, J. Kim, G. S. Park, M. G. Kim, Y. H. Kim, S. K. Park, *Adv. Mater.* **2022**, *34*, 2108979.
[14] W. Wang, S. Gao, Y. Li, W. Yue, H. Kan, C. Zhang, Z. Lou, L. Wang, G. Shen, *Adv. Funct. Mater.* **2021**, *31*, 2101201.
[15] Y.-X. Hou, Y. Li, Z.-C. Zhang, J.-Q. Li, D.-H. Qi, X.-D. Chen, J.-J. Wang, B.-W. Yao, M.-X. Yu, T.-B. Lu, J. Zhang, *ACS Nano* **2021**, *15*, 1497.
[16] F. Zhou, Z. Zhou, J. Chen, T. H. Choy, J. Wang, N. Zhang, Z. Lin, S. Yu, J. Kang, H. S. P. Wong, Y. Chai, *Nat. Nanotechnol.* **2019**, *14*, 776.
[17] Z. Yuan, C. Zhou, Y. Tian, Y. Shu, J. Messier, J. C. Wang, L. J. Van De Burgt, K. Kountouriotis, Y. Xin, E. Holt, *Nat. Commun.* **2017**, *8*, 14051.
[18] J. Shi, J. Zhang, L. Yang, M. Qu, D. C. Qi, K. H. Zhang, *Adv. Mater.* **2021**, *33*, 2006230.
[19] S. Chen, Z. Lou, D. Chen, G. Shen, *Adv. Mater.* **2018**, *30*, 1705400.
[20] B. Wang, A. Thukral, Z. Xie, L. Liu, X. Zhang, W. Huang, X. Yu, C. Yu, T. J. Marks, A. Facchetti, *Nat. Commun.* **2020**, *11*, 2405.
[21] L. Chen, J.-W. Ye, H.-P. Wang, M. Pan, S.-Y. Yin, Z.-W. Wei, L.-Y. Zhang, K. Wu, Y.-N. Fan, C.-Y. Su, *Nat. Commun.* **2017**, *8*, 15985.
[22] Y. Qin, L.-H. Li, Z. Yu, F. Wu, D. Dong, W. Guo, Z. Zhang, J.-H. Yuan, K.-H. Xue, X. Miao, S. Long, *Adv. Sci.* **2021**, *8*, 2101106.
[23] S. M. Kwon, J. Y. Kwak, S. Song, J. Kim, C. Jo, S. S. Cho, S. J. Nam, J. Kim, G. S. Park, Y. H. Kim, *Adv. Mater.* **2021**, *33*, 2105017.
[24] Y. Zhang, L. Wang, Y. Lei, B. Wang, Y. Lu, Y. Yao, N. Zhang, D. Lin, Z. Jiang, H. Guo, *ACS Nano* **2022**, *16*, 20937.
[25] H. Luo, L. Liang, H. Cao, M. Dai, Y. Lu, M. Wang, *ACS Appl. Mater. Interfaces* **2015**, *7*, 17023.
[26] H. Fang, W. Hu, *Adv. Sci.* **2017**, *4*, 1700323.
[27] J. Hao, Y.-H. Kim, N. Habisreutinger Severin, P. Harvey Steven, M. Miller Elisa, M. Foradori Sean, S. Arnold Michael, Z. Song, Y. Yan, M. Luther Joseph, L. Blackburn Jeffrey, *Sci. Adv.* **2021**, *7*, eabf1959.
[28] Z. Lin, Q. Chen, Y. Yan, Y. Liu, E. Li, W. Yu, H. Chen, T. Guo, *IEEE Electron Device Lett.* **2021**, *42*, 1358.
[29] S. Dai, Y. Zhao, Y. Wang, J. Zhang, L. Fang, S. Jin, Y. Shao, J. Huang, *Adv. Funct. Mater.* **2019**, *29*, 1903700.
[30] C. M. Yang, T. C. Chen, D. Verma, L. J. Li, B. Liu, W. H. Chang, C. S. Lai, *Adv. Funct. Mater.* **2020**, *30*, 2001598.
[31] S. Wang, C. Chen, Z. Yu, Y. He, X. Chen, Q. Wan, Y. Shi, D. W. Zhang, H. Zhou, X. Wang, P. Zhou, *Adv. Mater.* **2019**, *31*, 1806227.
[32] J. Tao, D. Sarkar, S. Kale, P. K. Singh, R. Kapadia, *Nano Lett.* **2020**, *20*, 7793.
[33] J.-K. Han, D.-M. Geum, M.-W. Lee, J.-M. Yu, S. K. Kim, S. Kim, Y.-K. Choi, *Nano Lett.* **2020**, *20*, 8781.
[34] S. M. Kwon, S. W. Cho, M. Kim, J. S. Heo, Y. H. Kim, S. K. Park, *Adv. Mater.* **2019**, *31*, 1906433.
[35] T. J. Lee, K. R. Yun, S. K. Kim, J. H. Kim, J. Jin, K. B. Sim, D. H. Lee, G. W. Hwang, T. Y. Seong, *Adv. Mater.* **2021**, *33*, 2105485.
[36] G. Chen, H. Cao, J. Conradt, H. Tang, F. Rohrbein, A. Knoll, *IEEE Signal Process Mag* **2020**, *37*, 34.
[37] R. Yan, Q. Hong, C. Wang, J. Sun, Y. Li, *IEEE Trans. Comput.-Aided Des. Integr.* **2022**, *41*, 3000.
[38] P. Giannozzi, O. Andreussi, T. Brumme, O. Bunau, M. Buongiorno Nardelli, M. Calandra, R. Car, C. Cavazzoni, D. Ceresoli, M. Cococcioni, N. Colonna, I. Carnimeo, A. Dal Corso, S. de Gironcoli, P. Delugas, R. A. DiStasio, A. Ferretti, A. Floris, G. Fratesi, G. Fugallo, R. Gebauer, U. Gerstmann, F. Giustino, T. Gorni, J. Jia, M. Kawamura, H. Y. Ko, A. Kokalj, E. Küçükbenli, M. Lazzeri, et al., *J. Phys.: Condens. Matter* **2017**, *29*, 465901.
[39] W. Zhang, R. Hong, W. Qin, Y. Lv, J. Ma, L. Liao, K. Li, C. Jiang, *J. Phys.: Condens. Matter* **2022**, *34*, 404003.